Journal of Materials Chemistry C

ROYAL SOCIETY OF CHEMISTRY

PAPER

View Article Online
View Journal

Cite this: DOI: 10.1039/d1tc01482j

Isothermal crystallization and time-temperature-transformation diagram of the organic semiconductor 5,11-bis(triethylsilylethynyl)-anthradithiophene†

Liyang Yu, *[ab] Andrew M. Zeidell,[c] John E. Anthony,[d] Oana D. Jurchescu[c] and Christian Müller *[b]

Thermal annealing of organic semiconductors is critical for optimization of their electronic properties. The selection of the optimal annealing temperature –often done on a trial-and-error basis– is essential for achieving the most desired micro/nanostructure. While classical materials science relies on time-temperature-transformation (TTT) diagrams to predict such processing-structure relationships, this type of approach is yet to find widespread application in the field of organic electronics. In this work, we constructed a TTT diagram for crystallization of the widely studied organic semiconductor 5,11-bis(triethylsilylethynyl)anthradithiophene (TES-ADT) from its melt. Thermal analysis in the form of isothermal crystallization experiments showed distinctly different types of behaviour depending on the annealing temperature, in agreement with classical crystal nucleation and growth theory. Hence, the TTT diagram correlates with the observed variation in the number of crystal domains, the crystal coverage and film texture as well as the obtained polymorph. As a result, we are able to rationalize the influence of the annealing temperature on the charge-carrier mobility extracted from field-effect transistor (FET) measurements. Evidently, the use of TTT diagrams is a powerful tool to describe structure formation of organic semiconductors and can be used to predict processing protocols that lead to optimal device performance.

Received 31st March 2021,
Accepted 12th July 2021

DOI: 10.1039/d1tc01482j

rsc.li/materials-c

1. Introduction

Thermal annealing is one of the most versatile and widely used post-deposition treatments for optimization of the micro/nanostructure of organic semiconductor thin films. The active layers of organic electronic and optoelectronic devices such as organic field-effect transistors (FETs)[1,2] and organic solar cells[3,4] are often subjected to thermal annealing to improve their crystallinity and, in turn, their charge transport ability. This is particularly true for small molecule semiconductors whose ability to transport electronic charge is governed by the thin-film micro/nanostructure.[5] For example, grain boundaries can strongly impede charge transport in FETs.[6–12] On the other hand, processing parameters that increase the crystal size may lead to the development of polymorphs that are associated with a lower charge-carrier mobility.[13–20] Changes in molecular packing due to polymorphism[14,18] and orientation[21] can also be a source for low device reproducibility. Thermal annealing is typically carried out by first placing the thin-film device onto a heated surface for a certain period of time, followed by cooling to room temperature. This process is akin to isothermal crystallization at a certain annealing temperature (T_{anneal}).[22] Annealing is to be carried out in a temperature range where crystallization can proceed, *i.e.* between the glass transition temperature (T_g) and melting temperature (T_m) of the material (or more specifically of the desired polymorph).[23]

A prominent example is thermal annealing of thin films that comprise fullerene derivatives. Mild annealing below the T_g can facilitate the formation of percolating pathways in polymer:fullerene bulk-heterojunction solar cells.[4,24,25] Instead, annealing above the T_g of the polymer:fullerene blend results in the growth of micrometre-sized fullerene crystals that impair the device performance.[26,27] In case of fullerene based FETs, crystallization can result in a dramatic improvement in charge-carrier mobility.[28,29] Carful selection of T_{anneal} was also

[a] School of Chemical Engineering, Sichuan University, Chengdu 610064, P. R. China. E-mail: liyangy@chalmers.se
[b] Department of Chemistry and Chemical Engineering, Chalmers University of Technology, 41296 Gothenburg, Sweden. E-mail: christian.muller@chalmers.se
[c] Department of Physics and Center for Functional Materials, Wake Forest University, Winston-Salem, NC 27109, USA
[d] Center for Applied Energy Research, University of Kentucky, Lexington, KY 40511, USA

† Electronic supplementary information (ESI) available. See DOI: 10.1039/d1tc01482j

found to be critical for the development of an optimal nanostructure in case of organic solar cells based on non-fullerene acceptors such as indacenodithienothiophene derivatives.[30] Another extensively studied molecular semiconductor that is often subjected to thermal annealing is rubrene. The selection of T_{anneal} was found to influence the starting time of crystal nucleation[31] as well as the crystal growth rate,[32,33] which has a pronounced impact on the crystal size as well as the polymorph that forms.[34,35] Deposition of rubrene together with the vitrification agent 9,10-diphenylanthracene can, upon thermal annealing, lead to extraordinary crystal quality and hence a high charge-carrier mobility.[35]

In the majority of cases thermal annealing of organic semiconductor thin films is done at an arbitrary temperature. Hence, it is of utmost importance to develop means that allow to rationalize how T_{anneal} influences the resulting micro/nanostructure, and to guide the selection of annealing parameters. A number of tools such as classical nucleation theory[36] and Avrami analysis[37] are available to predict optimal isothermal crystallization protocols.[38,39] Classical nucleation theory was found to describe isothermal crystallization of 5,11-bis(triethylsilylethynyl)anthradithiophene (TES-ADT) thin films.[31] Avrami analysis was used to characterise the isothermal crystallization process of TES-ADT as well as poly(3-(2′-ethyl)hexylthiophene) (P3EHT).[37,40] Another tool that is widely used in classical materials science – time–temperature–transformation (TTT) diagrams – is yet to find widespread use in the field of organic electronics. Only few reports exist that use TTT diagrams to rationalize the amorphous-to-crystal transformation process of organic semiconductors.[25,40] TTT diagrams not only describe the kinetics of isothermal crystallization but also lend predictive power with regard to the micro/nanostructure that develops during isothermal as well as non-isothermal crystallization of thin films.

In this report we establish the TTT diagram that describes crystallization of TES-ADT from its melt. We chose TES-ADT as a model material because it is a well-studied small molecule semiconductor,[16,18,41–43] and can be thermally annealed in air at relatively low temperatures to access its γ-phase without the risk for thermal degradation. Additionally, amorphous thin films of TES-ADT can be readily prepared by simply cooling molten films to room temperature, which provides reproducible samples for isothermal crystallization experiments.[44] We find that the TTT diagram is in excellent agreement with the observed variations in micro/nanostructure and correlates with the evolution of the charge-carrier mobility extracted from FETs.

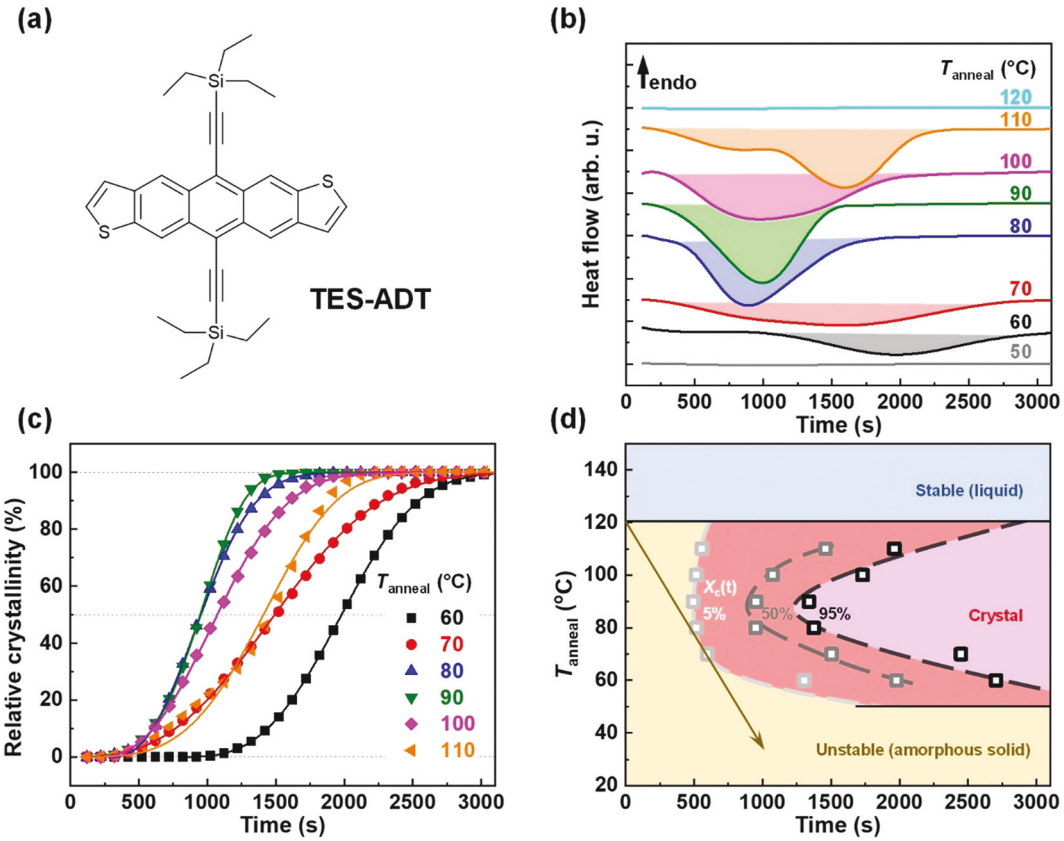

Fig. 1 (a) Chemical structure of TES-ADT. (b) Isothermal DSC thermograms of TES-ADT recorded during annealing at various T_{anneal}. (c) Relative crystallinity $X_c(t)$ as a function of time t (symbols) and best fits with the Avrami equation (solid lines). (d) Time-temperature-transformation (TTT) diagram displaying the time for $X_c(t)$ to reach 5%, 50% and 95%. The arrow represents the slowest constant-rate cooling process that results in a close to amorphous solid with $X_c(t) \approx 5\%$ (cooling rate ≈ -0.083 °C s^{-1}).

2. Results and discussion

2.1. Thermal analysis and bulk crystallization kinetics

TES-ADT (see Fig. 1a for chemical structure) displays a rich phase behaviour that entails several crystalline forms,[55] which dictates the annealing protocol that must be chosen in order to carry out meaningful isothermal crystallization experiments. The α-phase, which exhibits the highest field-effect mobilities, can be accessed by solution casting at low temperatures,[43] solvent-assisted crystallization[42] or solvent vapour annealing.[44] The β-phase has the highest melting temperature T_m of 155 °C and the γ-phase forms through cold crystallization from the melt around 100 °C.[18,45] The glass transition temperature T_g of TES-ADT is 27 °C.[44]

Isothermal crystallization experiments were carried out with differential scanning calorimetry (DSC). The DSC experiments presented in Fig. 1 were carried out with the same sample of TES-ADT quenched from its melt, which allowed us to ensure that each measurement commenced from a fully amorphous state. While samples solidified from solution would more closely mimic processing schemes used for the preparation of thin-film devices, the use of new samples for each DSC experiment may affect the reproducibility of our measurements. We chose the following experimental procedure. First, TES-ADT was heated to 155 °C and kept at this temperature for 5 min to ensure that the material is fully molten. Then, the molten material was cooled at a rate of −100 °C min^{-1} to T_{anneal} and kept at this temperature for 1 h. Note that a cooling rate of −10 °C min^{-1} has been reported to result in fully amorphous TES-ADT.[18] This cycle was repeated with the same sample while T_{anneal} was varied from 50 °C to 120 °C. A single broad exothermic peak due to cold crystallization for T_{anneal} between 60 °C to 110 °C was observed (Fig. 1b). In case of annealing at 60 °C, crystallization started after 1200 s and finished after about 3000 s. Instead, for T_{anneal} = 80–100 °C crystallization commenced almost instantly. The DSC isotherm recorded for T_{anneal} = 110 °C displayed two exotherms suggesting two crystallization events. No crystallization was observed at T_{anneal} = 50 °C and 110 °C in the bulk DSC sample, which we explain with the vicinity to the T_g and T_m, respectively.

We also investigated how the thermal history prior to T_{anneal} influences the crystallization kinetics. A sample directly cooled from 155 °C to T_{anneal} = 80 °C displayed a very similar DSC isotherm and hence comparable crystallization kinetics as the same material first cooled to 20 °C followed by heating to T_{anneal} = 80 °C (Fig. S1 and Table S1, ESI†). We therefore argue that the preparation protocol of the later on discussed thin-film samples, which involved a cooling step to room temperature prior to annealing, did not influence crystallization.

To calculate the relative degree of crystallinity $X_c(t)$ as a function of time (Fig. 1c) we integrated the DSC isotherms to obtain the partial enthalpy $\Delta H(t)$, which we normalized by the total enthalpy $\Delta H^0 = \lim_{t\to\infty} \Delta H(t)$ of each exotherm:

$$X_c(t) = \frac{\Delta H(t)}{\Delta H^0} \quad (1)$$

All calculations were carried out with weight–fraction crystallinity instead of volume–fraction crystallinity, which is required by the Avrami model, because the densities of the γ-phase (ρ = 1.128 ± 0.006 g cm^{-3}) and amorphous TES-ADT (ρ = 1.115 ± 0.004 g cm^{-3}) are very similar.[18] We constructed a TTT diagram (Fig. 1d) by plotting, for each T_{anneal}, the times at which the relative crystallinity had reached a value of $X_c(t)$ = 5%, 50% and 95%, which was used as an approximation for the time needed for the crystallization process to commence (t_{onset}), to be half complete (t_{mid}) and to finish (t_{endset}), as summarised in Table 1. The three corresponding isocrystalline lines in Fig. 1d have the typical bell shape that is common for TTT diagrams. The TTT diagram provides an overview of the crystallization process of TES-ADT in the bulk. We found that t_{onset} showed only a weak temperature dependence for T_{anneal} > 60 °C as the nucleation started almost instantly. Crystallization proceeds most rapidly at intermediate temperatures with $X_c(t)$ reaching 50% and then 95% most quickly at 80–90 °C and slows down towards lower or higher temperatures. We explain this behaviour with the influence of T_{anneal} on crystal nucleation and growth. Crystallization at temperatures close to T_g is limited by diffusion of molecules to the growing crystal and therefore we conclude that annealing at 60 °C or below is hampered by slow diffusion, leading to an increase in the time needed for crystallization. Instead, crystallization at temperatures close to T_m is limited by a low driving force for the formation of crystal nuclei, leading to the absence of any crystallization at $T_{anneal} \geq$ 120 °C.

To study the crystallization process of TES-ADT in more detail, we fitted the evolution of $X_c(t)$ with the Avrami equation (Fig. 1c):[34]

$$X_c(t) = 1 - \exp\left[-\left(\frac{t - t_0}{\tau}\right)^m\right] \quad (2)$$

where t_0 is the crystallization lag time, τ is a time constant and m is the Avrami coefficient. We obtained good fits for T_{anneal} = 60–100 °C, while the presence of a double peak in the isotherm at T_{anneal} = 110 °C resulted in a poor fit. For T_{anneal} > 60 °C we find that t_0 = 0 (Table 1), which suggest instant nucleation. The lowest τ value, which represents the maximum crystallization rate, was observed at $T_{max} \sim$ 80 °C, in agreement with the TTT diagram. The Avrami coefficients m deduced at T_{anneal} < 80 °C and T_{anneal} = 100 °C had a value of about 3 (Table 1). TES-ADT tends to undergo homogeneous nucleation in which case the Avrami coefficient corresponds to $m = D + 1$ where D is the dimensionality of crystal growth.[31] Hence, the isothermal annealing experiments described here, which were done with bulk material in a DSC pan, lead to two-dimensional growth of TES-ADT crystallites. For T_{anneal} = 80 and 90 °C, the

Table 1 Summary of parameters describing the crystallization kinetics obtained from thermal analysis

T_{anneal} (°C)	ΔH° (J g^{-1})	t_{onset} (s)	t_{mid} (s)	t_{endset} (s)	t_0 (s)	τ (s)	m
60	11.4	1303	1980	2705	800	1330	3.07
70	19.0	597	1503	2450	0	1697	2.82
80	23.6	516	949	1375	0	1059	3.53
90	24.0	493	952	1338	0	1036	4.12
100	22.3	516	1072	1730	0	1216	3.08
110	25.2	557	1461	1963	—	—	—

m values increased and reached 4 at T_{anneal} = 90 °C suggesting that three-dimensional crystallization occurs at T_{anneal} where TES-ADT crystallizes most rapidly. Crystal nuclei can readily form just above the T_g = 27 °C and, therefore, the onset of crystallization can proceed relatively unhindered at most investigated annealing temperatures but T_{anneal} < 60 °C where crystallization is sufficiently hampered by slow diffusion. The Avrami analysis further supported the findings inferred from the TTT diagram.

Hence, we conclude from the TTT diagram that the fastest crystal growth during isothermal crystallization of TES-ADT is at T_{max} ~ 80 °C. Below T_{max} crystallization is hampered by slow long-range molecular diffusion, while above T_{max} crystallization is limited by a low driving force for the formation of crystal nuclei. Hence, we refer to the temperature range between T_g and T_{max} as the diffusion limited (DL) region; and the temperature range between T_{max} and T_m as the nucleation limited (NL) region. The cooling line illustrating a non-isothermal crystallization process at a constant cooling rate of −0.083 °C s^{-1} forms a tangent to the iso-crystalline line representing the onset of crystallization ($X_c(t)$ = 5%, *cf.* Fig. 1d). This cooling rate represents a lower limit for bulk TES-ADT to be quenched to an amorphous solid from its melt, which agrees with a previous report where a cooling rate of −10 °C min^{-1} (−0.167 °C s^{-1}) allowed to fully quench molten material into an amorphous solid.[18]

2.2. Crystallization of TES-ADT thin films

To elucidate to which extent the TTT diagram established with DSC for bulk material correlates with the crystallization process of TES-ADT thin films, we thermally annealed a series of thin films immediately after fabrication and evaluated their properties. We spin-coated amorphous thin films with a thickness of about 50 nm onto silicon wafers from a 50 °C toluene solution of 10 g L^{-1} TES-ADT, followed by melting of samples for 5 min at 155 °C and subsequent quenching to room temperature on a large metal plate kept at room temperature. The elevated solution temperature was selected to prevent crystallization.[46] Thin-film samples were annealed at T_{anneal} = 30–130 °C in the dark for 1 h and quenched to room temperature on a large metal plate kept at room temperature. All thin film preparation was performed at ambient atmosphere. Optical microscopy revealed plate-like crystal structures in thin films annealed for 1 h at T_{anneal} = 30–110 °C (Fig. 2a). For T_{anneal} < 80 °C, *i.e.* the DL region, we observe a high crystal coverage of more than 85% and 500–1400 crystal domains per mm^2 (Fig. 2b). The high crystal coverage at 30–40 °C is in stark contrast to isothermal DSC measurements, which did not show any crystallization at these temperatures (*cf.* Fig. 1). We argue that the substrate and/or air interfaces provide heterogeneous nucleation sites, which together with confinement induced crystallization[47,48] permit crystallization already at lower temperatures. For T_{anneal} ≥ 80 °C, *i.e.* the NL region, the crystal size gradually increases from ~70 μm at T_{anneal} = 80 °C to over 300 μm at T_{anneal} = 110 °C while the number of crystal domains per unit area and the crystal coverage decreases significantly. Clear bell shapes can be found for both the number of crystal domains and the crystal coverage, which resemble the TTT diagram constructed for bulk material annealed in DSC pans (*cf.* Fig. 1b). Furthermore, in the DL region above T_{max}, a higher crystal coverage and fewer crystal domains were observed as compared to the NL region. We also notice distinct colour and brightness variations within almost every crystal domain in case of thin films annealed at high temperatures, *e.g.* T_{anneal} = 110 °C, suggesting that these crystal sheets are twisted. TES-ADT crystallites are relatively "soft" and bending has been observed for both α-[49] and β-phase crystals.[18]

To obtain additional insight into the influence of T_{anneal} on the crystal structure, grazing-incidence wide-angle X-ray scattering (GIWAXS) was performed on these thin films. The GIWAXS pattern (Fig. 3a) recorded for a thin film annealed at T_{anneal} = 60 °C showed clear out-of-plane (100), (200) and (300) diffractions corresponding to the γ-phase of TES-ADT. At T_{anneal} = 80 °C the intensity of these diffractions significantly increased, and an additional (400) diffraction appeared. For T_{anneal} = 100 °C, the diffraction intensity somewhat decreased, which is in agreement with the reduced film coverage observed with optical microscopy (Fig. 2). The intensities of diffractions recorded for a thin film annealed at 120 °C were further reduced with only a faint (100) diffraction visible. The highest

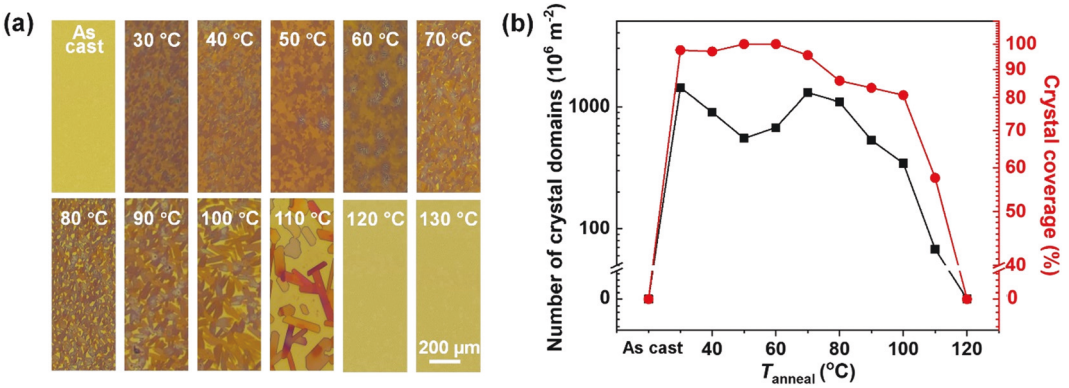

Fig. 2 (a) Polarized optical microscopy images recorded with two polarizers placed at an angle of 45° (not fully crossed) of TES-ADT thin films annealed at various temperatures and (b) number of crystal domains per area and crystal coverage extracted from the optical micrographs.

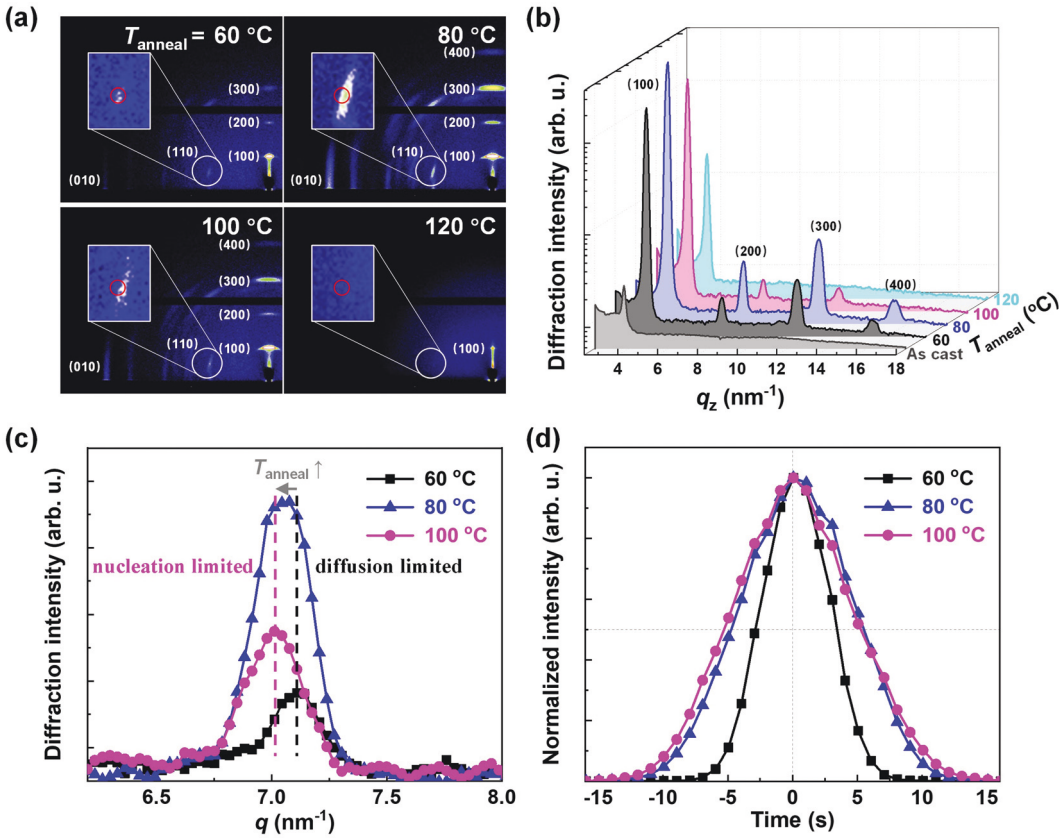

Fig. 3 (a) GIWAXS patterns of TES-ADT thin films annealed at various temperatures with the (110) diffractions highlighted and enlarged in the insets. (b) Vertical line cuts of (a) depicting the out-of-plane (h00) diffractions. (c) Comparison of the (110) diffraction of thin films annealed in the diffusion limited (DL) and nucleation limited (NL) region, which gives rise to slight variations of the γ-phase. (d) Azimuthal distribution of the (100) diffraction.

intensities for the (h00) out-of-plane diffractions were observed for T_{anneal} = 80 °C (Fig. 3b), which corresponds to T_{max} as suggested by the TTT diagram. We note that for T_{anneal} = 60 °C and 100 °C the relative intensity of the (h00) diffractions differs, suggesting differences in microstructure between the two thin films. Note that Lee *et al.* have reported that TES-ADT thin films crystallize slowly when kept at room temperature.[50] Since the here studied thin films were prepared a few days before the synchrotron measurements, weak (100) diffractions were observed for T_{anneal} = 120 °C as well as the unannealed reference film. All (h00) diffractions observed are out-of-plane suggesting that the molecules within the crystals are oriented predominately edge-on.

Annealing in the DL and NL regions resulted in slight differences in crystal packing. Examination of the (110) diffractions (compared in Fig. 3c and highlighted in Fig. 3a) revealed that the diffraction peak position shifts at higher T_{anneal} towards lower diffraction angles. While annealing in the DL as well as the NL region results in the growth of γ-phase crystals, we argue that slight differences in unit cell occur, which we label as the γ_{DL}- and γ_{NL}-phase, respectively. We also observed azimuthal broadening of the (100) diffraction for higher T_{anneal} (Fig. 3c). In contrast to the thin film annealed at 60 °C, thin films annealed at 80 °C and 100 °C show significantly broader diffractions. We calculated the Herman's orientation factor of the (100) diffraction and obtained values of 0.99, 0.95 and 0.94, respectively, which indicates that the degree of edge-on orientation decreased with T_{anneal}. The broadening of the azimuthal distribution of the (100) diffraction observed for the γ_{NL}-phase is consistent with the crystal sheet twisting inferred from optical micrographs (see Fig. 2). Furthermore, we analysed the in-plane crystal coherence length (CCL) of the (010) diffraction by means of the Scherrer equation.[51] Even though the crystal size increased with T_{anneal}, the CCL calculated for the thin films annealed at 60, 80 and 100 °C was 8.2, 7.4 and 7.0 nm, respectively. The CCL was a few orders of magnitude smaller than the domain size, which is not surprising when considering the "soft" nature of TES-ADT crystals.[18,49]

2.3. Charge-carrier mobility from FET devices

FET devices with a TES-ADT active layer were fabricated in bottom-gate, bottom-contact configuration and subjected to annealing at various temperatures (see Fig. 4 and Fig. S2, ESI†). The charge-carrier mobility (μ_{FET}) was extracted from the FET transfer characteristics in the saturation regime following standard procedures (Fig. 4a).[52] For the case of non-ideal devices, the mobility was estimated in a conservative way, using the lowest slope of this graph, as indicated with the red line. At least 20 samples were evaluated for each annealing procedure

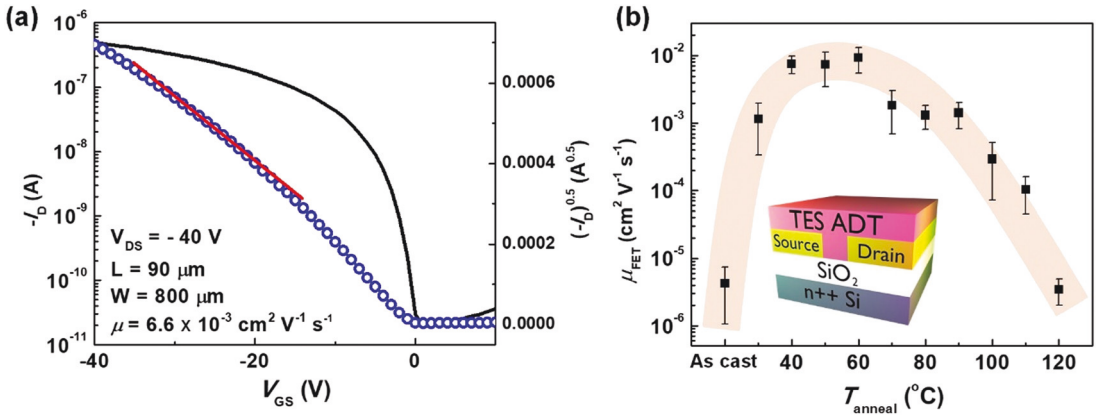

Fig. 4 (a) Transfer characteristics of a FET device with a TES-ADT active layer annealed at 60 °C. (b) saturation mobility of FET devices (μ_{FET}) annealed at various temperatures.

and the results were consistent. The spin-coated FET devices were briefly heated to 155 °C for 5 s and quenched by placing on a metal surface kept at room temperature for 5 s before immediate annealing at a given T_{anneal} for 1 h in the dark similar to the thin films. As-quenched thin films displayed a $\mu_{FET} < 10^{-5}$ cm^2 V^{-1} s^{-1}. In contrast, thin films annealed at 30 °C, which is only a few degrees above the T_g = 27 °C of TES-ADT, already display a drastically higher mobility of about 10^{-3} cm^2 V^{-1} s^{-1}. We obtained the highest μ_{FET} values of $(1 \pm 0.4) \times 10^{-2}$ cm^2 V^{-1} s^{-1} for devices annealed at 40–60 °C. At higher T_{anneal} between 70–90 °C, the μ_{FET} decreased to about $(1 \pm 0.7) \times 10^{-3}$ cm^2 V^{-1} s^{-1}. For $T_{anneal} \geq 100$ °C, we observe a significant reduction in μ_{FET}. In summary, the mobility varies over three orders of magnitude depending on the annealing temperature. We assign the poor performance of devices with an as-quenched active layer and those annealed at 120 °C to the amorphous nature of TES-ADT, in agreement with previous reports.[18,44,50] The evolution of μ_{FET} with T_{anneal} displayed a clear bell shape akin to the TTT diagram constructed from DSC thermograms (see Fig. 1). We extracted values of $\mu_{FET} \sim 10^{-2}$ cm^2 V^{-1} s^{-1} for devices annealed in the temperature range where crystallization –according to the TTT diagram– is most pronounced, while μ_{FET} decreased at both higher and lower temperatures. We attribute the slightly higher μ_{FET} values observed for the γ_{DL}-phase to the higher film coverage, which reduced the width of grain boundaries. In the high temperature regime, the reduction in mobility results from the decrease in coverage (Fig. 2b), as well as the reduction in crystallinity and content of the high mobility edge-on phase (Fig. 3). A longer annealing time is expected to increase the crystal coverage within the NL region, which would have a positive impact on the charge-transport mobility. The evolution of the subthreshold slope (S) with the annealing temperature can be described as a rotated "bell-shape", where a high mobility coincides with a small S, while the threshold slope is hardly affected by the annealing temperature (Fig. S4, ESI†). These observations suggest that the changes in film nanostructure modify the relatively deep trap environment, which are detected in S.[53]

3. Conclusions

In this work, we have studied the isothermal crystallization behaviour of the semiconducting small molecule TES-ADT using thermal analysis, which allowed the construction of a TTT diagram. For $T_{anneal} \geq 70$ °C nucleation of the γ-phase crystal of TES-ADT occurs instantaneously in the bulk, as confirmed by Avrami analysis. The crystal growth rate, however, was limited at temperatures close to the T_g and T_m due to limited molecular diffusion and a low driving force for crystallization, respectively. The fastest crystallization temperature was found at $T_{max} \sim 80$ °C. In contrast to bulk samples, nucleation more readily took place even at lower T_{anneal} in case of thin films, which we attribute to surface nucleation and confinement induced crystallization. The number of crystals per area, the crystal coverage, crystallinity and saturation mobility of TES-ADT thin films followed the same bell-shape trend displayed by the TTT diagram. Furthermore, we have identified two temperature regions below and above T_{max}. Thin films annealed in the diffusion limited region (T_g to T_{max}) and nucleation limited region (T_{max} to T_m), displayed clear differences in crystal size and coverage as well as slight variations in the unit cell of γ-phase crystals. We conclude that TTT diagrams are powerful tools that allow to predict the evolution of the micro/nanostructure and hence the electronic performance of organic semiconductors when subjected to thermal annealing. It can be anticipated that TTT diagrams will also allow to investigate how aspects such as the miscibility, phase separation and the crystallization sequence influence the solidification behaviour of semiconductor blends.

4. Experimental section

4.1. Materials

TES-ADT was synthesised according to a previously described method.[54] Toluene was purchased from Sigma Aldrich (Anhydrous, 99.8%) and used as received.

4.2. Differential scanning calorimetry (DSC)

DSC measurements were performed under nitrogen using a Mettler Toledo DSC 2 equipped with a high-sensitivity sensor (HSS9+). The samples (~5 mg) were placed into 20 μL Al crucible light sample pans. The samples were firstly molten at 155 °C and kept at the same temperature for 5 minutes, followed by a rapid cooling at rate of −100 °C min^{-1} to T_{anneal} = 50–120 °C to ensure that a fully amorphous structure is obtained,[18] subsequently, the isotherms were recorded for a duration of 1 h.

4.3. Thin film preparation

Thin films used in this work were prepared by spin-coating a 50 °C toluene solution containing 10 g L^{-1} TES-ADT onto silicon wafers to achieve amorphous thin films.[47] The thin films were thermally treated by sequentially placing on a hotplate kept at 155 °C for 5 min, followed by quenching on a large metal plate kept at room temperature for 5 s, transferring onto another hotplate kept at T_{anneal} = 30–130 °C for 1 h in the dark and quenching back to room temperature on a large metal plate kept at room temperature.

4.4. Optical microscopy

Images were taken with a Zeiss Axio Scope A1 equipped with a pair of polarizers placed at an angle of 45°.

4.5. Grazing-incidence wide-angle X-ray scattering (GIWAXS)

Measurements were conducted at the D-line of the Cornell High Energy Synchrotron Source (CHESS) at Cornell University. Thin films prepared on silicon wafers were placed on a sample stage where an X-ray was directed onto the sample surface with an incidence angle of 0.15° for 10 s. A Pilatus 200k area detector was placed 177.2 mm away from the sample stage to collect the scattered X-ray patterns.

4.6. Organic field-effect transistors (FETs)

FETs were prepared with bottom-gate bottom-contact configuration. Contacts consisting of 45 nm gold on 5 nm titanium were evaporated on silicon wafers with a 200 nm SiO_2 layer prior to the deposition of the TES-ADT layer by spin-coating a TES-ADT solution (10 g L^{-1}, 50 °C in toluene). The device channel lengths varied between 30 μm and 100 μm, and the channel width varied between 200 μm to 1000 μm. The as-deposited thin films were briefly heated to 155 °C for 5 s and quenched to room temperature before annealed at a given T_{anneal} for 1 h in the dark. The transfer and output characteristics were obtained from these devices using an Agilent 4155C Semiconductor Parameter Analyser. The fabrication, annealing and measurements of FET devices were conducted in a N_2 filled glove box. Square root values of the drain current from the transfer characteristics were used to extract the saturation mobility (μ_{FET}).

Conflicts of interest

There are not conflicts to declare.

Acknowledgements

We gratefully acknowledge funding from the Knut and Alice Wallenberg Foundation through the project ''Mastering Morphology for Solution-borne Electronics''. L. Y. thanks the National Natural Science Foundation of China (NSFC, 21905185) and the Fundamental Research Funds for the Central Universities (YJ201957) for financial support. The authors thanks CHESS (supported by NSF Award DMR-1332208) for providing experimental time for GIWAXS measurements. The work at WFU was supported by the National Science Foundation under awards DMR-1627925 and ECCS-1810273.

References

1 C. Reese, M. Roberts, M. Ling and Z. Bao, *Mater. Today*, 2004, **7**, 20–27.
2 H. Sirringhaus, *Adv. Mater.*, 2009, **21**, 3859–3873.
3 O. Inganäs, *Adv. Mater.*, 2018, **30**, 1800388.
4 A. J. Heeger, *Adv. Mater.*, 2014, **26**, 10–28.
5 S. S. Lee and Y. L. Loo, *Annu. Rev. Chem. Biomol. Eng.*, 2010, **1**, 59–78.
6 L. H. Jimison, M. F. Toney, I. McCulloch, M. Heeney and A. Salleo, *Adv. Mater.*, 2009, **21**, 1568–1572.
7 J. Rivnay, L. H. Jimison, J. E. Northrup, M. F. Toney, R. Noriega, S. Lu, T. J. Marks, A. Facchetti and A. Salleo, *Nat. Mater.*, 2009, **8**, 952–958.
8 L. Yu, X. Li, J. Smith, S. Tierney, R. Sweeney, B. K. C. C. Kjellander, G. H. Gelinck, T. D. Anthopoulos and N. Stingelin, *J. Mater. Chem.*, 2012, **22**, 9458–9461.
9 X. Li, A. Kadashchuk, I. I. Fishchuk, W. T. T. Smaal, G. Gelinck, D. J. Broer, J. Genoe, P. Heremans and H. Bässler, *Phys. Rev. Lett.*, 2012, **108**, 066601.
10 A. K. Hailey, S. Y. Wang, Y. Chen, M. M. Payne, J. E. Anthony, V. Podzorov and Y. L. Loo, *Adv. Funct. Mater.*, 2015, **25**, 5662–5668.
11 S. Anand, K. P. Goetz, Z. A. Lamport, A. M. Zeidell and O. D. Jurchescu, *Appl. Phys. Lett.*, 2019, **115**, 073301.
12 Y. Mei, D. Fogel, J. Chen, J. W. Ward, M. M. Payne, J. E. Anthony and O. D. Jurchescu, *Org. Electron.*, 2017, **50**, 100–105.
13 Y. Yuan, G. Giri, A. L. Ayzner, A. P. Zoombelt, S. C. B. Mannsfeld, J. Chen, D. Nordlund, M. F. Toney, J. Huang and Z. Bao, *Nat. Commun.*, 2014, **5**, 3005.
14 Y. Diao, B. C.-K. Tee, G. Giri, J. Xu, D. H. Kim, H. A. Becerril, R. M. Stoltenberg, T. H. Lee, G. Xue, S. C. B. Mannsfeld and Z. Bao, *Nat. Mater.*, 2013, **12**, 665–671.
15 S. Galindo, A. Tamayo, F. Leonardi and M. Mas-Torrent, *Adv. Funct. Mater.*, 2017, **27**, 1700526.
16 K. Paudel, G. Giesbers, J. Van Schenck, J. E. Anthony and O. Ostroverkhova, *Org. Electron.*, 2019, **67**, 311–319.
17 Z. A. Lamport, K. J. Barth, H. Lee, E. Gann, S. Engmann, H. Chen, M. Guthold, I. McCulloch, J. E. Anthony, L. J. Richter, D. M. DeLongchamp and O. D. Jurchescu, *Nat. Commun.*, 2018, **9**, 5130.

18 L. Yu, X. Li, E. Pavlica, F. P. V. V. Koch, G. Portale, I. da Silva, M. A. Loth, J. E. Anthony, P. Smith, G. Bratina, B. K. C. C. Kjellander, C. W. M. M. Bastiaansen, D. J. Broer, G. H. Gelinck and N. Stingelin, *Chem. Mater.*, 2013, **25**, 1823–1828.
19 G. Giri, R. Li, D.-M. Smilgies, E. Q. Li, Y. Diao, K. M. Lenn, M. Chiu, D. W. Lin, R. Allen, J. Reinspach, S. C. B. Mannsfeld, S. T. Thoroddsen, P. Clancy, Z. Bao and A. Amassian, *Nat. Commun.*, 2014, **5**, 3573.
20 L. A. Stevens, K. P. Goetz, A. Fonari, Y. Shu, R. M. Williamson, J.-L. Brédas, V. Coropceanu, O. D. Jurchescu and G. E. Collis, *Chem. Mater.*, 2015, **27**, 112–118.
21 R. Li, J. W. Ward, D. M. Smilgies, M. M. Payne, J. E. Anthony, O. D. Jurchescu and A. Amassian, *Adv. Mater.*, 2012, **24**, 5553–5558.
22 S. Malik and A. K. Nandi, *J. Polym. Sci., Part B: Polym. Phys.*, 2002, **40**, 2073–2085.
23 C. Müller, *Chem. Mater.*, 2015, **27**, 2740–2754.
24 B. C. Thompson and J. M. J. Fréchet, *Angew. Chem., Int. Ed.*, 2008, **47**, 58–77.
25 J. Bergqvist, C. Lindqvist, O. Bäcke, Z. Ma, Z. Tang, W. Tress, S. Gustafsson, E. Wang, E. Olsson, M. R. Andersson, O. Inganäs and C. Müller, *J. Mater. Chem. A*, 2014, **2**, 6146–6152.
26 C. Lindqvist, A. Sanz-Velasco, E. Wang, O. Bäcke, S. Gustafsson, E. Olsson, M. R. Andersson and C. Müller, *J. Mater. Chem. A*, 2013, **1**, 7174–7180.
27 S. Bertho, G. Janssen, T. J. Cleij, B. Conings, W. Moons, A. Gadisa, J. D'Haen, E. Goovaerts, L. Lutsen, J. Manca and D. Vanderzande, *Sol. Energy Mater. Sol. Cells*, 2008, **92**, 753–760.
28 T. D. Anthopoulos, D. M. De Leeuw, E. Cantatore, S. Setayesh, E. J. Meijer, C. Tanase, J. C. Hummelen and P. W. M. Blom, *Appl. Phys. Lett.*, 2004, **85**, 4205–4207.
29 T. D. Anthopoulos, D. M. de Leeuw, E. Cantatore, P. van't Hof, J. Alma and J. C. Hummelen, *J. Appl. Phys.*, 2005, **98**, 054503.
30 L. Yu, D. Qian, S. Marina, F. A. A. Nugroho, A. Sharma, S. Hultmark, A. I. Hofmann, R. Kroon, J. Benduhn, D.-M. Smilgies, K. Vandewal, M. R. Andersson, C. Langhammer, J. Martín, F. Gao, C. Müller, J. Mart, F. Gao and C. Mu, *ACS Appl. Mater. Interfaces*, 2019, **11**, 21766–21774.
31 L. Yu, M. R. Niazi, G. O. Ngongang Ndjawa, R. Li, A. R. Kirmani, R. Munir, A. H. Balawi, F. Laquai and A. Amassian, *Sci. Adv.*, 2017, **3**, e1602462.
32 T. R. Fielitz and R. J. Holmes, *Cryst. Growth Des.*, 2016, **16**, 4720–4726.
33 M. A. Fusella, S. Yang, K. Abbasi, H. H. Choi, Z. Yao, V. Podzorov, A. Avishai and B. P. Rand, *Chem. Mater.*, 2017, **29**, 6666–6673.
34 H. M. Lee, H. Moon, H. S. Kim, Y. N. Kim, S. M. Choi, S. Yoo and S. O. Cho, *Org. Electron. Phys., Mater. Appl.*, 2011, **12**, 1446–1453.
35 N. Stingelin-Stutzmann, E. Smits, H. Wondergem, C. Tanase, P. Blom, P. Smith and D. de Leeuw, *Nat. Mater.*, 2005, **4**, 601–606.
36 D. Turnbull and J. C. Fisher, *J. Chem. Phys.*, 1949, **17**, 71–73.
37 M. Avrami, *J. Chem. Phys.*, 1940, **8**, 212–224.
38 N. Van den Brande, G. Van Assche and B. Van Mele, *Polymer*, 2015, **57**, 39–44.
39 B. S. Beckingham, V. Ho and R. A. Segalman, *ACS Macro Lett.*, 2014, **3**, 684–688.
40 L. Yu, E. Davidson, A. Sharma, M. R. Andersson, R. Segalman and C. Müller, *Chem. Mater.*, 2017, **29**, 5654–5662.
41 S. S. Lee, C. S. Kim, E. D. Gomez, B. Purushothaman, M. F. Toney, C. Wang, A. Hexemer, J. E. Anthony and Y. L. Loo, *Adv. Mater.*, 2009, **21**, 3605–3609.
42 J. Chen, M. Shao, K. Xiao, A. J. Rondinone, Y.-L. Loo, P. R. C. Kent, B. G. Sumpter, D. Li, J. K. Keum, P. J. Diemer, J. E. Anthony, O. D. Jurchescu and J. Huang, *Nanoscale*, 2014, **6**, 449–456.
43 L. Yu, X. Li, E. Pavlica, M. A. Loth, J. E. Anthony, G. Bratina, C. Kjellander, G. Gelinck and N. Stingelin, *Appl. Phys. Lett.*, 2011, **99**, 5–8.
44 K. C. Dickey, J. E. Anthony and Y. L. Loo, *Adv. Mater.*, 2006, **18**, 1721–1726.
45 K. Muhieddine, R. W. Lyttleton, J. Badcock, M. A. Loth, J. A. Stride, J. E. Anthony and A. P. Micolich, *J. Org. Semicond.*, 2014, **2**, 7–14.
46 L. Yu, X. Li, E. Pavlica, M. A. Loth, J. E. Anthony, G. Bratina, C. Kjellander, G. Gelinck and N. Stingelin, *Appl. Phys. Lett.*, 2011, **99**, 263304.
47 J. Balko, A. Rinscheid, A. Wurm, C. Schick, R. H. Lohwasser, M. Thelakkat and T. Thurn-Albrecht, *J. Polym. Sci., Part B: Polym. Phys.*, 2016, **54**, 1791–1801.
48 Z. Mencik, H. K. Plummer and H. Van Oene, *J. Polym. Sci., Part A-2*, 1972, **10**, 507–517.
49 S. S. Lee, J. M. Mativetsky, M. A. Loth, J. E. Anthony and Y. L. Loo, *ACS Nano*, 2012, **6**, 9879–9886.
50 W. H. Lee, J. A. Lim, D. H. Kim, J. H. Cho, Y. Jang, Y. H. Kim, J. I. Han and K. Cho, *Adv. Funct. Mater.*, 2008, **18**, 560–565.
51 D.-M. Smilgies, *J. Appl. Crystallogr.*, 2009, **42**, 1030–1034.
52 Z. A. Lamport, H. F. Haneef, S. Anand, M. Waldrip and O. D. Jurchescu, *J. Appl. Phys.*, 2018, **124**, 071101.
53 H. F. Haneef, A. M. Zeidell and O. D. Jurchescu, *J. Mater. Chem. C*, 2020, **8**, 759–787.
54 M. M. Payne, S. R. Parkin, J. E. Anthony, C. C. Kuo and T. N. Jackson, *J. Am. Chem. Soc.*, 2005, **127**, 4986–4987.
55 L. Yu, G. Portale and N. Stingelin, *J. Mater. Chem. C*, 2021, DOI: 10.1039/d1tc01418h.

